

Surface warming and wetting due to methane's long-wave radiative effects muted by short-wave absorption

Received: 26 August 2022

Accepted: 9 February 2023

Published online: 16 March 2023

 Check for updates

Robert J. Allen¹✉, Xueying Zhao¹, Cynthia A. Randles^{2,8}, Ryan J. Kramer^{3,4}, Bjørn H. Samset⁵ & Christopher J. Smith^{6,7}

Although greenhouse gases absorb primarily long-wave radiation, they also absorb short-wave radiation. Recent studies have highlighted the importance of methane short-wave absorption, which enhances its stratospherically adjusted radiative forcing by up to ~15%. The corresponding climate impacts, however, have been only indirectly evaluated and thus remain largely unquantified. Here we present a systematic, unambiguous analysis using one model and separate simulations with and without methane short-wave absorption. We find that methane short-wave absorption counteracts ~30% of the surface warming associated with its long-wave radiative effects. An even larger impact occurs for precipitation as methane short-wave absorption offsets ~60% of the precipitation increase relative to its long-wave radiative effects. The methane short-wave-induced cooling is due largely to cloud rapid adjustments, including increased low-level clouds, which enhance the reflection of incoming short-wave radiation, and decreased high-level clouds, which enhance outgoing long-wave radiation. The cloud responses, in turn, are related to the profile of atmospheric solar heating and corresponding changes in temperature and relative humidity. Despite our findings, methane remains a potent contributor to global warming, and efforts to reduce methane emissions are vital for keeping global warming well below 2 °C above preindustrial values.

The atmospheric concentration of methane (CH₄) has increased by about a factor of 2.4 since preindustrial times (from -0.75 to 1.8 parts per million by volume (ppm)), resulting in an effective radiative forcing (ERF; Methods) of $0.496 \pm 0.099 \text{ W m}^{-2}$ (from 1850 to 2019)¹, with similar estimates based on the stratospherically adjusted radiative forcing (SARF; Methods)^{2–4}. Due to methane's

potency as a greenhouse gas (its global warming potential is 27.9 times that of CO₂ on a 100 yr time horizon⁵), its relatively short lifetime (~1 decade) and chemical reactions in the atmosphere (for example, tropospheric ozone production), considerable interest exists in targeting CH₄ emissions to mitigate climate change and to improve air quality^{4,6–13}.

¹Department of Earth and Planetary Sciences, University of California, Riverside, CA, USA. ²ExxonMobil Technology and Engineering Company, Annandale, NJ, USA. ³Climate and Radiation Laboratory, NASA Goddard Space Flight Center, Greenbelt, MD, USA. ⁴Goddard Earth Science Technology and Research II, University of Maryland at Baltimore County, Baltimore, MD, USA. ⁵CICERO Center for International Climate and Environmental Research in Oslo, Oslo, Norway. ⁶School of Earth and Environment, University of Leeds, Leeds, UK. ⁷International Institute for Applied Systems Analysis (IIASA), Laxenburg, Austria. ⁸Present address: UNEP International Methane Emission Observatory, Paris, France. ✉e-mail: rjallen@ucr.edu

Recent studies^{14–17} have highlighted the importance of CH₄ short-wave (SW) absorption at near-infrared wavelengths—which is lacking in many climate models¹—resulting in up to an ~15% increase in its SARF compared with the long-wave (LW) SARF¹⁹. A more recent study²⁰ found a smaller increase in SARF, at 7%, which was attributed, in part, to the inclusion of CH₄ absorption of solar mid-infrared radiation in the 7.6- μm -band spectral region. The reduced forcing is because this spectral region impacts mainly stratospheric absorption. CH₄ SW absorption has regional ‘hotspots’, including near bright surfaces (for example, deserts) and above clouds (for example, oceanic stratus cloud decks)²¹. Such bright regions enhance the upward reflection of sunlight, which in turn enhances top-of-the-atmosphere (TOA) and tropopause CH₄ SW instantaneous radiative forcing (IRF). Considerable uncertainty exists, however, as this forcing depends on several quantities, including the cloud radiative effect, CH₄ vertical profile²⁰ and surface albedo specification²⁰. In particular, large spatial gradients in the SW forcing are caused by near-infrared surface albedo²¹.

These studies focus largely on how CH₄ SW absorption impacts its radiative forcing, with some also addressing the corresponding rapid adjustments (ADJs, surface-temperature-independent responses). For example, CO₂ and CH₄ (with SW absorption) fixed sea surface temperatures (SST) and slab ocean simulations were compared to show that ADJs associated with CH₄ SW radiative effects act to mute precipitation increases¹⁶ due to enhanced warming of the upper troposphere and lower stratosphere (UTLS). Methane SW ADJs were also investigated in Precipitation Driver and Response Model Intercomparison Project (PDRMIP)²² simulations. Models that lack CH₄ SW absorption yield a positive overall ADJ (acting to increase net energy into the climate system), whereas models that include CH₄ SW absorption yield a negative overall ADJ (acting to increase net energy out of the climate system)¹⁸. This difference is due to a more negative tropospheric temperature adjustment and negative as opposed to positive stratospheric and cloud adjustments in models that include CH₄ SW absorption. These negative adjustments, in turn, are consistent with stronger UTLS warming, which promotes enhanced outgoing LW radiation to space and high-level cloud reductions, which further promote enhanced outgoing LW radiation. Although other model differences (for example, cloud parameterizations and CH₄ vertical profile) may impact this result, the implication is that CH₄ SW absorption may not lead to additional surface warming.

Although the importance of CH₄ SW absorption has been recognized, a comprehensive (and systematic) analysis of how it impacts the climate system remains to be conducted. In this study, we perform experiments to rigorously assess CH₄ SW radiative impacts on the climate system, including ADJs, surface-temperature-mediated feedbacks and the overall climate response.

Results

A suite of idealized methane-only time-slice perturbation simulations (Table 1 and Methods) are conducted with the National Center for Atmospheric Research Community Earth System Model version 2.1.3 (CESM2)²³. CESM2 includes the newest model components, including the Community Atmosphere Model version 6 (CAM6). Unlike many climate models¹⁸, CAM6 includes CH₄ SW absorption in the near-infrared bands except the mid-infrared band in its radiative transfer parameterization. For each methane perturbation (2 \times , 5 \times and 10 \times preindustrial atmospheric CH₄ concentrations) considered and ocean boundary condition (fixed climatological sea surface temperatures, fSST, versus coupled ocean), we conduct pairs of identical experiments, one that includes CH₄ LW + SW radiative effects and one that lacks CH₄ SW radiative effects (Table 1). This allows quantification of the response signals (relative to preindustrial CH₄) to CH₄ LW + SW, LW and SW radiative effects, abbreviated as CH_{4LW+SW}, CH_{4LW} and CH_{4SW}, respectively. Under radiative transfer experiments (Methods), CH₄ radiative effects include the IRF only (the initial perturbation to the radiation balance).

Table 1 | Description of CESM2/CAM6 methane experiments

Experiment	Description
10 \times CH ₄ ^{EXP}	10 \times CH ₄ with CH ₄ LW + SW radiative effects ^a
10 \times CH ₄ ^{EXP} _{NOSW}	10 \times CH ₄ with CH ₄ SW radiative effects turned off (LW effects) ^a
PI ^{EXP}	Preindustrial CH ₄ with CH ₄ LW + SW radiative effects
PI ^{EXP} _{NOSW}	Preindustrial CH ₄ with SW radiative effects turned off (LW effects)
Signal	Description
10 \times CH _{4LW+SW} = 10 \times CH ₄ ^{EXP} - PI ^{EXP}	Response to CH ₄ LW + SW radiative effects ^b
10 \times CH _{4LW} = 10 \times CH ₄ ^{EXP} _{NOSW} - PI ^{EXP} _{NOSW}	Response to CH ₄ LW radiative effects ^b
10 \times CH _{4SW} = (10 \times CH ₄ ^{EXP} - PI ^{EXP}) - (10 \times CH ₄ ^{EXP} _{NOSW} - PI ^{EXP} _{NOSW})	Response to CH ₄ SW radiative effects ^b

Top half of the table displays model experiments; bottom half displays response signals (difference of experiments). Atmospheric methane concentrations are perturbed relative to the preindustrial (PI=year 1850) concentration; 10 \times CH₄ (preindustrial) represents 7.9 (0.79) ppm. Experiments are performed with both fixed climatological sea surface temperatures and a coupled ocean. The former allows quantification of the ADJs/fast responses; the latter allows quantification of the total climate response. The difference (total climate response minus fast response) quantifies the slow, surface-temperature-mediated feedback response. ^aAnalogous sets of simulations are also conducted for both 5 \times CH₄ (3.95 ppm) and 2 \times CH₄ (1.58 ppm). ^bRadiative effects include IRF for radiative transfer simulations; IRF and ADJs—which can be LW and SW adjustments—for fSST simulations; and IRF, ADJs and feedbacks for coupled simulations.

Under fSST experiments, CH₄ radiative effects can induce an ERF, which includes both the IRF and ADJs (change in state in response to IRF, but excluding changes in sea surface temperatures). Rapid adjustments can be LW adjustments (for example, tropospheric and stratospheric temperatures), SW adjustments (surface albedo) or both SW and LW adjustments (clouds). The coupled ocean–atmosphere experiments quantify the total climate response, including the IRF, ADJs and the slow, surface-temperature-mediated effects.

Methane SW versus LW total climate responses

Figure 1 shows the global mean change in near-surface air temperature and precipitation in coupled ocean–atmosphere CESM2 simulations, which is the total response (including IRF, adjustments and surface-temperature-mediated feedbacks) to increases in atmospheric methane concentrations, including 2 \times CH₄, 5 \times CH₄ and 10 \times CH₄ relative to preindustrial (see also Extended Data Figs. 1 and 2). For all three perturbations, CH_{4LW}—which represents the total climate response to methane LW IRF, adjustments and feedbacks—yields an increase in near-surface air temperature and precipitation (warming and ‘wetting’). Significant global mean warming of 0.09, 0.68 and 1.24 K occurs for 2 \times CH_{4LW}, 5 \times CH_{4LW} and 10 \times CH_{4LW}; similarly, global wetting of 0.001 (not significant at the 90% confidence level), 0.035 and 0.063 mm d⁻¹ occurs (corresponding precipitation changes are 0.04, 1.2 and 2.1%). Interestingly, CH_{4LW+SW}—which represents the total climate response to methane LW + SW IRF, adjustments and feedbacks—yields muted warming and wetting (except for 2 \times CH_{4LW+SW}). This is due to SW effects (including the IRF, adjustments and feedbacks), where significant global cooling occurs for 5 \times CH_{4SW} and 10 \times CH_{4SW} at -0.23 and -0.39 K. Similarly, a significant decrease in global mean precipitation occurs under these two methane perturbations at -0.021 and -0.039 mm d⁻¹ (-0.7 and -1.3%). Most of the precipitation decrease occurs over tropical oceans (for example, Extended Data Fig. 2c).

The decrease in precipitation is consistent with atmospheric energetic constraints—in the global mean, the primary balance is between net atmospheric radiative cooling and condensational heating from precipitation^{16,24–26}. As atmospheric SW absorption increases, net radiative cooling decreases, which is consistent with a decrease in

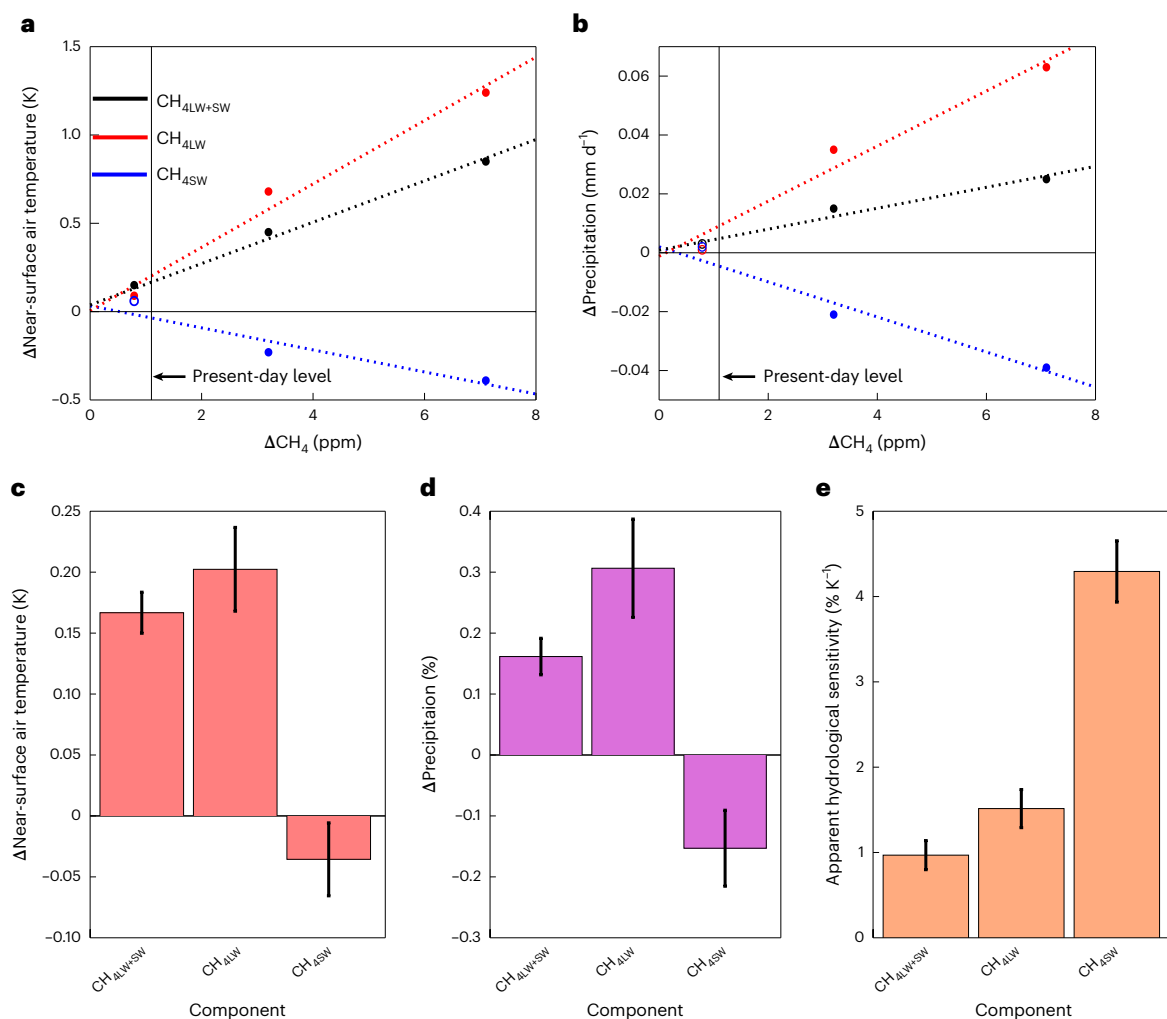


Fig. 1 | Total climate response to methane perturbations. **a, b**, Global annual mean near-surface air temperature (**a**) and precipitation (**b**) response for $2\times\text{CH}_4$ (0.79 ppm), $5\times\text{CH}_4$ (3.16 ppm) and $10\times\text{CH}_4$ (7.11 ppm) from coupled simulations (which include the IRF, adjustments and feedbacks). Responses are decomposed into $\text{CH}_{4\text{LW}+\text{SW}}$, $\text{CH}_{4\text{LW}}$ and $\text{CH}_{4\text{SW}}$. Also included are the least-squares regression lines (dotted). Solid circles represent a significant response at the 90% confidence level, based on a standard *t* test. The thin black vertical line

shows the present-day CH_4 perturbation of 1.1 ppm. **c–e**, The estimated (from the regressions) present-day CH_4 climate responses for near-surface air temperature (**c**), precipitation (**d**) and apparent hydrological sensitivity (**e**). Except for **e**, the $\text{CH}_{4\text{LW}+\text{SW}}$ bar is equal to the sum of the $\text{CH}_{4\text{LW}}$ and $\text{CH}_{4\text{SW}}$ bars. Error bars in **c–e** show the 1 s.d. uncertainty estimate of the regression slope, which is estimated from the three like-coloured data points (CAM6 methane simulations) in **a** and **b**. The error-bar centre is the regression-estimated response.

precipitation. Except for the $2\times\text{CH}_4$ perturbation, $\text{CH}_{4\text{SW}}$ offsets over $\sim 30\%$ of the surface warming and $\sim 60\%$ of the wetting associated with $\text{CH}_{4\text{LW}}$; that is, SW absorption offsets twice as much of the precipitation increase, compared with the surface warming.

We estimate the present-day CH_4 climate response (ΔCH_4 of 1.1 ppm) from least-squares regressions applied to our idealized $2\times\text{CH}_4$, $5\times\text{CH}_4$ and $10\times\text{CH}_4$ simulations (Fig. 1a,b). Figure 1c shows the corresponding near-surface air temperature response, decomposed into $\text{CH}_{4\text{LW}+\text{SW}}$, $\text{CH}_{4\text{LW}}$ and $\text{CH}_{4\text{SW}}$. We find global warming of 0.17 K in response to present-day CH_4 (relative to preindustrial); this is decomposed into warming of 0.20 K from $\text{CH}_{4\text{LW}}$ and -0.04 K (cooling) from $\text{CH}_{4\text{SW}}$. Our estimate of 0.17 K for $\text{CH}_{4\text{LW}+\text{SW}}$ is less than that given in the newest IPCC report (based on 2019 relative to 1750 and a two-layer emulator) at 0.28 K, with a 5–95% range of 0.19 to 0.39 K (ref. 1) (discussed in Supplementary Note 1). For global mean precipitation (Fig. 1d), precipitation increases of 0.16% and 0.31% occur for $\text{CH}_{4\text{LW}+\text{SW}}$ and $\text{CH}_{4\text{LW}}$, respectively; a precipitation decrease of -0.15% occurs under $\text{CH}_{4\text{SW}}$. The apparent hydrological sensitivities (defined as the change in precipitation divided by the change in surface temperature)²⁷ are 0.97, 1.51 and $4.30\% \text{ K}^{-1}$ for $\text{CH}_{4\text{LW}+\text{SW}}$, $\text{CH}_{4\text{LW}}$ and $\text{CH}_{4\text{SW}}$, respectively

(Fig. 1e; discussed in Supplementary Note 2). Our decomposition helps to explain the larger apparent hydrological sensitivity to methane found in PDRMIP models (many of which lack CH_4 SW radiative effects; discussed in Supplementary Note 2).

Radiative flux components

To understand the cause of the $\text{CH}_{4\text{SW}}$ surface cooling in coupled simulations, we evaluate the radiative flux components (Methods)—including ERF, IRF and the ADJs—in the fSST experiments. Figure 2a shows the TOA radiative flux components in response to $10\times\text{CH}_{4\text{LW}+\text{SW}}$, $10\times\text{CH}_{4\text{LW}}$ and $10\times\text{CH}_{4\text{SW}}$. The IRF is 2.08 W m^{-2} , with $10\times\text{CH}_{4\text{LW}}$ and $10\times\text{CH}_{4\text{SW}}$ both contributing positive values at 1.81 and 0.27 W m^{-2} , respectively. Thus, the $10\times\text{CH}_{4\text{SW}}$ IRF increases the $10\times\text{CH}_{4\text{LW}}$ IRF by 15% (13% for $5\times\text{CH}_4$ and $2\times\text{CH}_4$). A previous study found a similar 15% increase under a 750–1,800 ppb CH_4 perturbation²⁰. A smaller increase of 6% was found at the tropopause¹⁹, but the partitioning of SW IRF and LW IRF at the tropopause will differ from the TOA¹⁷. We also note that the presence of clouds increases the $10\times\text{CH}_{4\text{SW}}$ IRF from 0.20 W m^{-2} under clear-sky conditions to 0.27 W m^{-2} under all-sky conditions (a 35% increase; $5\times\text{CH}_{4\text{SW}}$ and $2\times\text{CH}_{4\text{SW}}$ yield 27% and 33% increases, respectively). The increased

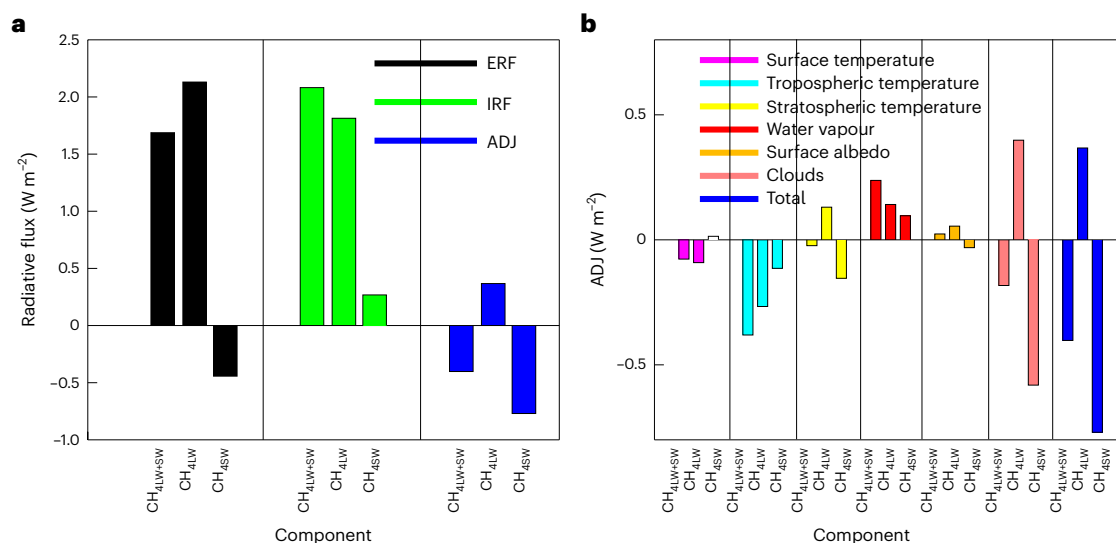


Fig. 2 | TOA radiative flux components and ADJ decomposition for 10×CH₄. **a**, Global annual mean TOA ERF, IRF and ADJ. **b**, Global annual mean TOA surface temperature, tropospheric temperature, stratospheric temperature, water

vapour, surface albedo, cloud and total ADJ for 10×CH₄. Responses that are not significant, based on a standard *t* test at the 90% confidence level, have unfilled bars.

forcing due to clouds is related to increased absorption path lengths in the CH₄ bands caused by multiple scattering^{19,21}.

The 10×CH₄SW+LW and 10×CH₄LW ERFs are also positive, at 1.69 and 2.13 W m⁻², respectively, but the 10×CH₄SW ERF is negative, at -0.44 W m⁻². Thus, 10×CH₄SW acts to reduce the 10×CH₄LW ERF by 21%. The difference between ERF and IRF is due to ADJs; 10×CH₄SW+LW yields a negative ADJ, at -0.40 W m⁻², which is due to the 10×CH₄SW of -0.77 W m⁻² (relative to the positive ADJ for 10×CH₄LW of 0.37 W m⁻²). Thus, 10×CH₄SW drives a strong negative ADJ, offsetting its smaller positive IRF (by a factor of ~3), leading to a negative ERF of -0.44 W m⁻². This 10×CH₄SW negative ERF is consistent with the corresponding decrease in near-surface air temperature previously discussed (Fig. 1). We note that some of the 10×CH₄SW adjustments are LW adjustments (discussed in ‘ADJ decomposition’).

Qualitatively similar results are obtained from 5×CH₄ and 2×CH₄ (Supplementary Note 3 and Extended Data Fig. 3). Atmospheric and surface radiation contributions to the TOA radiation (ERF) changes are discussed in Supplementary Note 4 (see also Supplementary Fig. 1).

ADJ decomposition

To further understand the ADJs and climate impacts of CH₄SW absorption, Fig. 2b shows the decomposition of TOA ADJs (for 10×CH₄) into the tropospheric temperature, stratospheric temperature, surface temperature, water vapour, albedo and cloud adjustment (Methods). Clouds are the main driver of the relatively large negative 10×CH₄SW ADJ. The corresponding cloud adjustment is -0.58 W m⁻², which is 75% of the total ADJ. The stratospheric temperature adjustment also contributes, at -0.15 W m⁻², as does the tropospheric temperature adjustment, at -0.11 W m⁻². The water-vapour adjustment—at 0.10 W m⁻²—acts to oppose these negative adjustments. The remaining ADJs, including surface temperature and albedo, are relatively small. Similar results are obtained for 5×CH₄ and 2×CH₄ (Extended Data Fig. 4).

The 10×CH₄SW cloud adjustment (Fig. 2b) is due to both SW radiation, at -0.42 W m⁻² (Extended Data Fig. 4c), and LW radiation, at -0.16 W m⁻² (Extended Data Fig. 4b). The corresponding 10×CH₄SW temperature and water-vapour adjustments are consistent with atmospheric warming (particularly in the UTLS; Fig. 3b), which leads to enhanced outgoing LW radiation (a negative LW adjustment; Extended Data Fig. 4b); the warming likewise increases water vapour (a greenhouse gas), which acts to decrease outgoing LW radiation (a positive LW

adjustment; Extended Data Fig. 4b). Supplementary Note 5 discusses the decomposition of surface (and atmospheric) ADJs for 10×CH₄ (see also Supplementary Fig. 2).

Recent analyses^{3,18} have shown similar results across different kernels^{28–30}, including the Geophysical Fluid Dynamics Laboratory kernel used here. Nonetheless, we repeat our ADJ calculations with the CloudSat/CALIPSO³⁰ radiative kernel and find similar results (Supplementary Note 6 and Extended Data Fig. 5).

Understanding the cloud adjustment

The negative 10×CH₄SW cloud adjustment—including negative TOA SW and LW contributions—is consistent with the change in the global mean vertical profile of cloud cover (Fig. 3d, dashed line). This includes increased low-level cloud cover (peaking at 800 hPa) and enhanced reflection of SW radiation (a negative adjustment) but decreased high-level cloud cover (peaking at 100 hPa) and enhanced outgoing LW radiation (a negative adjustment). The change in the vertical profile of cloud cover is related to the change in relative humidity (RH), which increases below -500 hPa but decreases aloft (Fig. 3c, dashed line). The corresponding correlation, *r*, from the surface up to the lower stratosphere (up to -100 hPa) is 0.86, suggesting an increase (decrease) in RH is associated with more (fewer) clouds. The change in RH is consistent with the change in the vertical profile of temperature (*r* = -0.76; Fig. 3b, dashed line), which in turn is related to the atmospheric SW heating rate (*r* = 0.88; 3a dashed line). Thus, we suggest the 10×CH₄SW cloud response is driven ultimately by the atmospheric SW heating-rate profile, which decreases in the low/mid troposphere (below -700 hPa) but increases aloft, peaking in the UTLS at 100 hPa. This is consistent with the traditionally defined aerosol–cloud semi-direct effect^{31–34}, whereby solar heating (for example, from black carbon) increases atmospheric temperature and decreases RH, leading to cloud burn-off (with the opposite occurring in the lower troposphere). Atmospheric cooling below -800 hPa and warming aloft also imply an increase in stability, which is also probably associated with the increase in low cloud cover. Similar responses occur under 5×CH₄ (Supplementary Fig. 3) and (although weaker) 2×CH₄ (Supplementary Fig. 4).

Atmospheric SW heating response profile

The global annual mean CH₄ instantaneous SW heating-rate response profile is not related to the vertical profile of the CH₄ concentration,

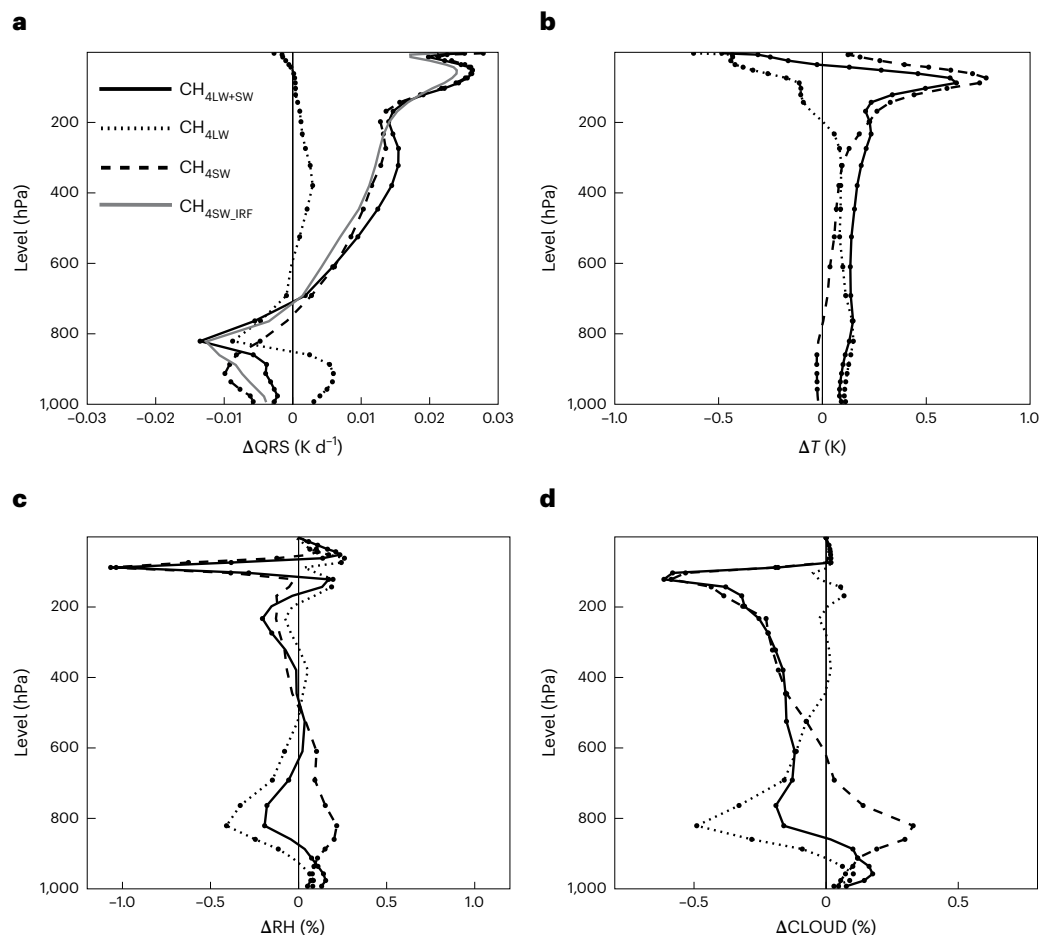


Fig. 3 | Global annual mean vertical profiles of fast responses for $10\times\text{CH}_4$. **a–d**, Atmospheric SW heating rate (QRS) (**a**), temperature (T) (**b**), relative humidity (RH) (**c**) and cloud fraction (CLOUD) (**d**) for $10\times\text{CH}_4$. Panels include the

contributions from $10\times\text{CH}_{4\text{LW}+\text{SW}}$, $10\times\text{CH}_{4\text{LW}}$ and $10\times\text{CH}_{4\text{SW}}$. Solid dots represent a significant response at the 90% confidence level, based on a standard *t* test. Also included in **a** is the instantaneous SW heating-rate profile ($10\times\text{CH}_{4\text{SW_IRF}}$).

which in CESM2/CAM6 has a uniform distribution in the troposphere (up to ~200 hPa) and then exponentially decreases aloft (Extended Data Fig. 6), consistent with chemical destruction of CH_4 above the tropopause. Instead, the instantaneous SW heating-rate response profile is related to overlap of the three CH_4 SW absorption bands with water vapour. Under clear-sky conditions, with water-vapour SW absorption in the three methane SW bands (Methods) turned off (using the Parallel Offline Radiative Transfer (PORT) model), the vertical profile of CH_4 SW instantaneous absorption is relatively uniform in the troposphere, peaking in the UTLS (Fig. 4a). Adding back the SW absorption by water vapour leads to the characteristic SW heating-rate response profile (as in Fig. 3a), with decreases in the lower troposphere and increases aloft, peaking in the UTLS. As expected, the $10\times\text{CH}_{4\text{SW}}$ clear-sky IRF increases (from 0.20 to 0.40 W m^{-2}) when the overlapping SW absorption by water vapour is turned off.

Since water vapour is at its maximum in the lower troposphere, these SW absorption bands are already highly saturated in the lower atmosphere at preindustrial CH_4 concentrations, so perturbing methane does not lead to an increase in SW heating here. However, methane SW radiative effects enhance SW absorption aloft (increase in SW heating rate). This reduces the amount of solar radiation in these three bands that can be subsequently absorbed by water vapour in the lower troposphere, which results in the SW heating-rate decrease below ~700 hPa. Similar results are obtained under all-sky conditions (Fig. 4b). The $10\times\text{CH}_{4\text{SW}}$ IRF increases (from 0.27 to 0.43 W m^{-2}) when the overlapping SW absorption by water vapour is turned off. Here, however, even

with water-vapour SW absorption (in the three methane bands) tuned off, there is still a decrease in the instantaneous SW heating rate near 800 hPa. This appears to be related to clouds, which peak at about the same level. Extended Data Fig. 7 shows similar plots but based on three different latitude bands: the low latitudes (30° S–30° N); mid-latitudes (30° N–60° N and 30° S–60° S) and the high latitudes (60° N–90° N and 60° S–90° S). There are some differences relative to the global mean (Fig. 4), but the results are generally similar. For example, absorption by water vapour (in the three methane bands) is more important in the low latitudes (Extended Data Fig. 7e), consistent with the larger amount of water vapour (specific humidity) in the tropics. To summarize, methane SW instantaneous radiative effects result in a vertical redistribution of atmospheric SW heating, with enhanced SW heating aloft (maximizing in the UTLS) but decreased SW heating in the lower troposphere. This, in turn, leads to the corresponding cloud-cover changes (increased low-level but decreased high-level cloud cover) and negative cloud adjustment, through modification of atmospheric temperature and relative humidity.

Climate feedbacks under methane SW radiative effects

Figure 5 shows the radiative kernel decomposition applied to the coupled ocean–atmosphere simulations for $10\times\text{CH}_{4\text{SW}}$ ($5\times\text{CH}_{4\text{SW}}$ and $2\times\text{CH}_{4\text{SW}}$ are included in Supplementary Fig. 5). We also include the previously discussed ADJs (‘fast’ responses from the fSST runs) and the difference between the coupled and fSST decompositions (the surface-temperature-induced ‘slow’ feedbacks). Note that we do not

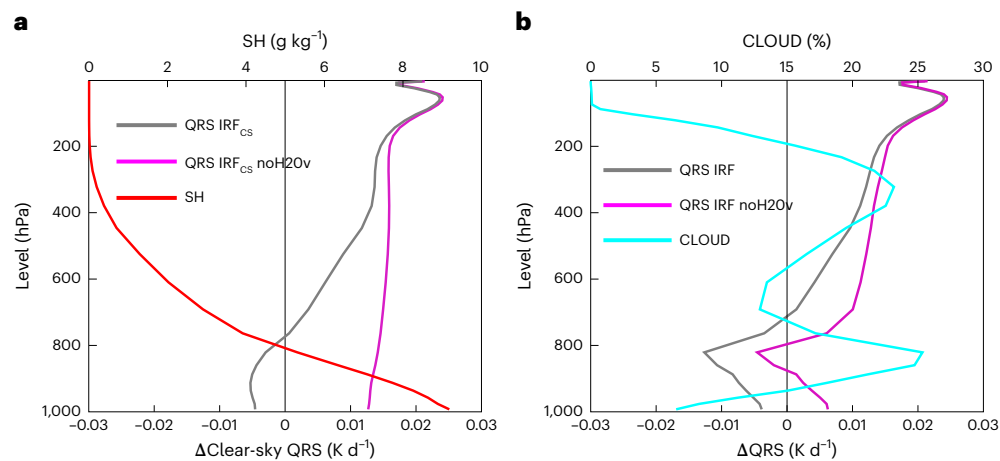


Fig. 4 | Global annual mean vertical profiles of instantaneous heating rate for $10\times\text{CH}_{4\text{SW}}$. **a**, Instantaneous atmospheric clear-sky SW heating rate (QRS IRF_{cs}) and the corresponding clear-sky SW heating rate without water-vapour SW absorption (QRS IRF_{cs} noH2Ov) in the same three near-infrared bands (1.6–1.9, 2.15–2.50 and 3.10–3.85 μm) that methane absorbs in.

Also includes the climatological SH. **b**, Instantaneous atmospheric all-sky (with clouds) SW heating rate (QRS IRF; as in Fig. 3a) and the corresponding SW heating rate without water-vapour SW absorption (QRS IRF noH2Ov) in the same three near-infrared bands that methane absorbs in. Also includes the climatological cloud fraction (CLOUD).

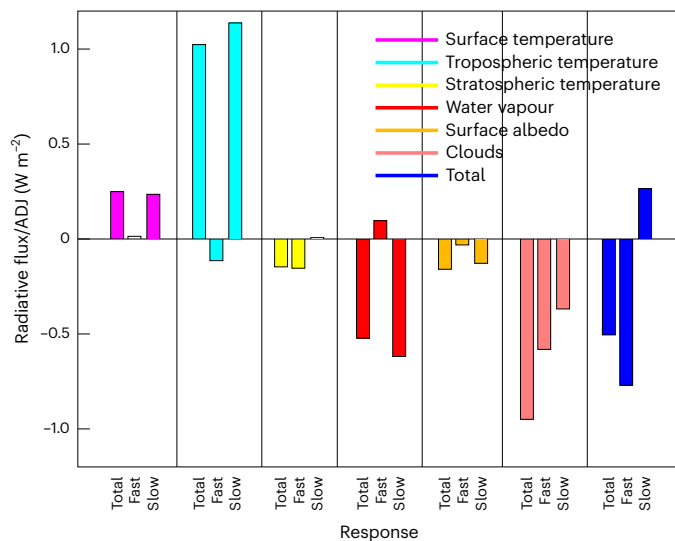


Fig. 5 | TOA radiative flux decomposition for the total response, ADJ and feedback for $10\times\text{CH}_{4\text{SW}}$. Global annual mean TOA surface temperature, tropospheric temperature, stratospheric temperature, water vapour, surface albedo, cloud and total radiative flux decomposition for $10\times\text{CH}_{4\text{SW}}$. The first bar in each like-coloured set of three bars represents the total response (from the coupled ocean simulations), the second bar represents the ADJ (fast response) and the third bar represents the surface-temperature-induced feedback (slow response). Responses not significant, based on a standard t test at the 90% confidence level, have unfilled bars. Units are W m^{-2} .

normalize our feedbacks by the change in global mean surface temperature; unnormalized feedbacks facilitate comparison with the ADJs. Thus, positive/negative feedbacks have the same meaning as positive/negative ADJs (positive is an increase in net energy; negative is a decrease in net energy).

In most cases, the slow feedback dominates the sign of the overall response, consistent with the climate system acting to restore TOA radiative equilibrium. For example, the slow tropospheric temperature feedback is positive at 1.14 W m^{-2} (which is offset to some extent by the water-vapour feedback at -0.62 W m^{-2}). Both of these feedbacks are consistent with tropospheric cooling (Supplementary Fig. 6b).

For clouds, however, the ADJ and the slow feedback are both negative, with a larger value for the ADJ, at -0.58 versus -0.37 W m^{-2} . Thus, the surface cooling in response to CH_4 SW radiative effects is due largely to cloud ADJs, but surface-temperature-induced cloud feedbacks also act to cool the planet.

The $10\times\text{CH}_{4\text{SW}}$ cloud feedback is dominated by increases in low-level (and mid-level) clouds, with weaker decreases in high-level clouds (Supplementary Fig. 6d and Supplementary Note 7). Similar results exist for $5\times\text{CH}_{4\text{SW}}$ (Supplementary Fig. 7), but weaker results exist for $2\times\text{CH}_{4\text{SW}}$ (Supplementary Fig. 8 and Supplementary Note 7).

Conclusions

Using targeted climate model simulations, we have shown that methane SW absorption and the associated ADJs act to reduce its ERF by $\sim 20\%$ and mute its warming and wetting effects in coupled simulations by up to 30% and 60%, respectively. Similar simulations with additional climate models are needed to understand the robustness of the results presented here—particularly since the CH_4 SW IRF is dependent on uncertain quantities, such as the cloud radiative effect²¹, the surface albedo^{20,21} and the CH_4 vertical profile²⁰. However, the indirect assessment of multiple models from PDRMIP CH_4 simulations supports our findings¹⁸. In fact, expanding on the results of ref. ¹⁸, we find a 20% decrease in ERF, 45% less warming and 65% less wetting in models that include CH_4 SW absorption versus those that do not (Supplementary Note 8 and Extended Data Fig. 8).

Although the SW radiative effects associated with the present-day methane perturbation remain relatively small, they could be quite large by the end of the century—Shared Socioeconomic Pathway 3–7.0, which lacks climate policy and has ‘weak’ levels of air-quality control measures^{7,35,36}, features end-of-century increases of CH_4 concentrations approaching $5\times$ preindustrial (3.4 ppm). Overall, methane remains a potent contributor to global warming, and emissions reductions are a vital component of climate change mitigation policies and for continued pursuit of the climate goals laid out under the Paris Agreement.

Online content

Any methods, additional references, Nature Portfolio reporting summaries, source data, extended data, supplementary information, acknowledgements, peer review information; details of author contributions and competing interests; and statements of data and code availability are available at <https://doi.org/10.1038/s41561-023-01144-z>.

References

- Forster, P. et al. in *Climate Change 2021: The Physical Science Basis* (eds Masson-Delmotte, V. et al.) 923–1054 (Cambridge Univ. Press, 2021).
- Myhre, G. et al. in *Climate Change 2013: The Physical Science Basis* (eds Stocker, T. F. et al.) Ch. 8 (Cambridge Univ. Press, 2013).
- Thornhill, G. D. et al. Effective radiative forcing from emissions of reactive gases and aerosols—a multi-model comparison. *Atmos. Chem. Phys.* **21**, 853–874 (2021).
- Szopa, S. et al. in *Climate Change 2021: The Physical Science Basis* (eds Masson-Delmotte, V. et al.) 817–922 (Cambridge Univ. Press, 2021).
- Smith, C. et al. in *Climate Change 2021: The Physical Science Basis* (eds Masson-Delmotte, V. et al.) Ch. 7 (Cambridge Univ. Press, 2021).
- Collins, W. J. et al. AerChemMIP: quantifying the effects of chemistry and aerosols in CMIP6. *Geosci. Model Dev.* **10**, 585–607 (2017).
- Allen, R. J. et al. Significant climate benefits from near-term climate forcer mitigation in spite of aerosol reductions. *Environ. Res. Lett.* **16**, 034010 (2021).
- Hayman, G. D. et al. Regional variation in the effectiveness of methane-based and land-based climate mitigation options. *Earth Syst. Dyn.* **12**, 513–544 (2021).
- Global Methane Assessment: Benefits and Costs of Mitigating Methane Emissions* (UNEP, 2021).
- Cain, M. et al. Methane and the Paris Agreement temperature goals. *Phil. Trans. A* **380**, 20200456 (2022).
- Mar, K. A., Unger, C., Walderdorff, L. & Butler, T. Beyond CO₂ equivalence: the impacts of methane on climate, ecosystems, and health. *Environ. Sci. Policy* **134**, 127–136 (2022).
- Turnock, S. T. et al. The future climate and air quality response from different near-term climate forcer, climate, and land-use scenarios using UKESM1. *Earths Future* **10**, e2022EFO02687 (2022).
- Hassan, T. et al. Air quality improvements are projected to weaken the Atlantic meridional overturning circulation through radiative forcing effects. *Commun. Earth Environ.* **3**, 149 (2022).
- Collins, W. D. et al. Radiative forcing by well-mixed greenhouse gases: estimates from climate models in the Intergovernmental Panel on Climate Change (IPCC) Fourth Assessment Report (AR4). *J. Geophys. Res. Atmos.* <https://doi.org/10.1029/2005JD006713> (2006).
- Li, J., Curry, C. L., Sun, Z. & Zhang, F. Overlap of solar and infrared spectra and the shortwave radiative effect of methane. *J. Atmos. Sci.* **67**, 2372–2389 (2010).
- Modak, A., Bala, G., Caldeira, K. & Cao, L. Does shortwave absorption by methane influence its effectiveness? *Clim. Dyn.* **51**, 3653–3672 (2018).
- Shine, K. P., Byrom, R. E. & Checa-Garcia, R. Separating the shortwave and longwave components of greenhouse gas radiative forcing. *Atmos. Sci. Lett.* **23**, e1116 (2022).
- Smith, C. J. et al. Understanding rapid adjustments to diverse forcing agents. *Geophys. Res. Lett.* **45**, 12023–12031 (2018).
- Etmann, M., Myhre, G., Highwood, E. J. & Shine, K. P. Radiative forcing of carbon dioxide, methane, and nitrous oxide: a significant revision of the methane radiative forcing. *Geophys. Res. Lett.* **43**, 12614–12623 (2016).
- Byrom, R. E. & Shine, K. P. Methane's solar radiative forcing. *Geophys. Res. Lett.* <https://doi.org/10.1029/2022GL098270> (2022).
- Collins, W. D., Feldman, D. R., Kuo, C. & Nguyen, N. H. Large regional shortwave forcing by anthropogenic methane informed by Jovian observations. *Sci. Adv.* **4**, eaas9593 (2018).
- Myhre, G. et al. PDRMIP: a Precipitation Driver and Response Model Intercomparison Project—protocol and preliminary results. *Bull. Am. Meteorol. Soc.* **98**, 1185–1198 (2017).
- Danabasoglu, G. et al. The Community Earth System Model version 2 (CESM2). *J. Adv. Model. Earth Syst.* **12**, e2019MS001916 (2020).
- Muller, C. J. & O’Gorman, P. A. An energetic perspective on the regional response of precipitation to climate change. *Nat. Clim. Change* **1**, 266–271 (2011).
- Richardson, T. B. et al. Drivers of precipitation change: an energetic understanding. *J. Clim.* **31**, 9641–9657 (2018).
- Liu, L. et al. A PDRMIP multimodel study on the impacts of regional aerosol forcings on global and regional precipitation. *J. Clim.* **31**, 4429–4447 (2018).
- Fläschner, D., Mauritsen, T. & Stevens, B. Understanding the intermodel spread in global-mean hydrological sensitivity. *J. Clim.* **29**, 801–817 (2016).
- Pendergrass, A. G., Conley, A. & Vitt, F. M. Surface and top-of-atmosphere radiative feedback kernels for CESM-CAM5. *Earth Syst. Sci. Data* **10**, 317–324 (2018).
- Smith, C. J., Kramer, R. J. & Sima, A. The HadGEM3-GA7.1 radiative kernel: the importance of a well-resolved stratosphere. *Earth Syst. Sci. Data* **12**, 2157–2168 (2020).
- Kramer, R. J., Matus, A. V., Soden, B. J. & L’Ecuyer, T. S. Observation-based radiative kernels from CloudSat/CALIPSO. *J. Geophys. Res. Atmos.* **124**, 5431–5444 (2019).
- Allen, R. J. & Sherwood, S. C. The aerosol–cloud semi-direct effect and land–sea temperature contrast in a GCM. *Geophys. Res. Lett.* **37**, L07702 (2010).
- Koch, D. & DelGenio, A. D. Black carbon semi-direct effects on cloud cover: review and synthesis. *Atmos. Chem. Phys.* **10**, 7685–7696 (2010).
- Amiri-Farahani, A., Allen, R. J., Li, K.-F. & Chu, J.-E. The semidirect effect of combined dust and sea salt aerosols in a multimodel analysis. *Geophys. Res. Lett.* **46**, 10512–10521 (2019).
- Allen, R. J. et al. Observationally-constrained aerosol–cloud semi-direct effects. *NPJ Clim. Atmos. Sci.* <https://doi.org/10.1038/s41612-019-0073-9> (2019).
- Fujimori, S. et al. SSP3: AIM implementation of shared socioeconomic pathways. *Glob. Environ. Change* **42**, 268–283 (2017).
- Gidden, M. J. et al. Global emissions pathways under different socioeconomic scenarios for use in CMIP6: a dataset of harmonized emissions trajectories through the end of the century. *Geosci. Model Dev.* **12**, 1443–1475 (2019).

Publisher’s note Springer Nature remains neutral with regard to jurisdictional claims in published maps and institutional affiliations.

Open Access This article is licensed under a Creative Commons Attribution 4.0 International License, which permits use, sharing, adaptation, distribution and reproduction in any medium or format, as long as you give appropriate credit to the original author(s) and the source, provide a link to the Creative Commons license, and indicate if changes were made. The images or other third party material in this article are included in the article’s Creative Commons license, unless indicated otherwise in a credit line to the material. If material is not included in the article’s Creative Commons license and your intended use is not permitted by statutory regulation or exceeds the permitted use, you will need to obtain permission directly from the copyright holder. To view a copy of this license, visit <http://creativecommons.org/licenses/by/4.0/>.

© The Author(s) 2023

Methods

Radiative-forcing definitions

The IRF is the initial perturbation to Earth's radiation budget and does not account for ADJs. We diagnose IRF using the PORT model³⁷, which isolates the Rapid Radiative Transfer Model for general circulation models (RRTMG)^{38,39} radiative transfer computation from the CESM2–CAM6 model configuration (more details on RRTMG are presented in 'CESM2/CAM6 simulations'). PORT simulations are run for 16 months; the last 12 months are used to diagnose annual mean IRF. PORT is also used to verify our methodology to remove RRTMG CH₄ SW absorption (the SW IRF is zero in the CH₄^{EXP}_{4NOSW} and PI^{EXP}_{NOSW} experiments, and the LW IRF is unchanged).

The ERF is defined as the net TOA radiative flux difference between the perturbed and base simulation, with climatological fixed SSTs and sea-ice distributions and no correction for land surface-temperature change⁴⁰. We note that the contribution of land surface warming/cooling to the ERF in our simulations is relatively small (<5% of the ERF; Supplementary Note 9). ERF can be decomposed into the sum of IRF and the ADJs.

The SARF is equal to the sum of the IRF and the stratospheric temperature adjustment. Thus, the difference between ERF and SARF is that ERF includes all adjustments, whereas SARF includes only the adjustment due to stratospheric temperature change^{2,41,42}.

CESM2/CAM6 simulations

We conduct pairs of identical simulations, one that includes CH₄ LW+SW radiative effects (CH₄^{EXP}) and one that lacks CH₄ SW radiative effects (CH₄^{EXP}_{4NOSW}; Table 1). The latter simulations are conducted by turning off CH₄ SW absorption in the three near-infrared bands—1.6–1.9 μm, 2.15–2.50 μm and 3.10–3.85 μm—in CAM6's radiative transfer parameterization (RRTMG). RRTMG does not include methane SW absorption in the mid-infrared band at 7.6 μm. The sign of the CH₄ SW IRF (at the tropopause) depends on the increased absorption in the troposphere since the downward SW flux at the tropopause is always decreased due to absorption in the stratosphere⁴⁹. Including the 7.6 μm band primarily increases CH₄ SW absorption in the stratosphere²⁰. This reduces the forcing from the downward irradiance, with negligible change to the forcing from the upward irradiance; that is, the tropopause SW IRF is reduced. Thus, if RRTMG included the 7.6 μm methane band, we would expect the CH₄ SW IRF at the TOA to increase due to the increase in stratospheric absorption. This, however, will result in a larger (negative) stratospheric temperature adjustment.

RRTMG is an accelerated and modified version of RRTM and uses the correlated *k*-distribution method to treat gas absorption³⁹. RRTMG calculates irradiance and heating rate in broad spectral intervals while retaining a high level of accuracy relative to measurements and high-resolution line-by-line models. Sub-grid cloud characterization is treated in both the LW and SW spectral regions with the Monte Carlo Independent Column Approximation⁴³ using the maximum–random cloud overlap assumption. RRTMG divides the solar spectrum into 14 SW bands that extend over the spectral range from 0.2 μm to 12.2 μm. The infrared spectrum in RRTMG is divided into 16 LW bands that extend over the spectral range from 3.1 μm to 1000.0 μm.

Few studies have evaluated broadband radiative transfer codes against benchmark calculations, particularly for CH₄ SW IRF. This is in part because the radiation parameterization in many climate models lacks an explicit treatment of CH₄ SW absorption^{14,18}. The 6-band SOCRATES SW spectral file configuration used in the Met Office Unified Model significantly underestimates CH₄ SW tropopause and surface IRF by around 45% compared with the 260-band configuration²⁰. Similarly, RRTMG—the radiative transfer model used here—was recently found to underestimate CH₄ (and CO₂) SW IRF by 25–45% (ref. 44). This implies that there are opportunities for improvement in the parts of the spectrum where the absorption by these gases is weak but not zero. Thus, incorporating CH₄ SW absorption in more models' radiative transfer

codes is only part of the solution—making sure their radiative transfer codes have a validated treatment of SW absorption by CH₄ (and other greenhouse gases) is also vital. We also note that N₂O is not represented in the SW part of RRTMG.

The Community Land Model version 5⁴⁵ provides both the surface albedo, area-averaged for each atmospheric column, and the upward LW surface flux, which incorporates the surface emissivity, for input to the radiation. For the SW, the surface albedos are specified at every grid point at every time step. The albedos are partitioned into two wavebands (0.2–0.7 μm and 0.7–12.0 μm) for both direct and diffuse incident radiation⁴⁶. Surface albedos for ocean surfaces, geographically varying land surfaces and sea-ice surfaces are distinguished. They depend on the solar zenith angle, the amount and optical properties of vegetation and the optical properties of snow and soil⁴⁵.

Rapid adjustments—which can be SW or LW adjustments—are estimated by subtracting the preindustrial control (PI^{EXP}) fSST experiment from each perturbation fSST experiment. For example, to quantify the ADJs in response to a tenfold increase in preindustrial atmospheric methane concentration, we take the 10×CH₄ fSST simulation minus the preindustrial fSST simulation (10×CH₄^{EXP} – PI^{EXP}). This signal (10×CH₄^{EXP}_{LW+SW}) includes the methane LW+SW IRF and its impact on LW and SW adjustments under the fSST boundary condition (ERF = IRF + adjustments). ADJs due to CH₄ LW IRF and its impact on LW and SW adjustments (10×CH₄^{EXP}_{LW}) are estimated from 10×CH₄^{EXP}_{4NOSW} – PI^{EXP}_{NOSW}. Similarly, ADJs due to CH₄ SW IRF and the impact of CH₄ SW absorption on LW and SW adjustments (10×CH₄^{EXP}_{SW}) are estimated from (10×CH₄^{EXP} – PI^{EXP}) – (10×CH₄^{EXP}_{4NOSW} – PI^{EXP}_{NOSW}). Specific details on how the ADJs are estimated (via radiative kernels) are discussed in 'Calculation of ADJs'. A similar procedure is used to quantify the total climate impacts from the coupled ocean simulations, which include the IRF, adjustments and surface-temperature-mediated feedbacks.

We note that an alternative experimental design where methane LW radiative effects are removed could be implemented. As our goal is to understand the impacts of adding CH₄ SW absorption (which many models lack) to the LW forcing (which models already have), our experimental design is based on the all-but-one type of experimental design. Our simulations therefore target the inclusion of CH₄ SW absorption, allowing quantification of its associated ADJs and climate impacts. This is in contrast to the studies discussed, which evaluate CH₄ SW radiative effects either by contrasting CH₄ versus CO₂ (which lacks strong SW absorption) simulations¹⁶ or by comparing models that include CH₄ SW absorption with models that do not¹⁸. In the latter, other model differences (for example, cloud parameterizations and CH₄ vertical profile) may be important.

All CESM2/CAM6 simulations are conducted with a 1.9° × 2.5° horizontal resolution and 32 vertical levels in the atmosphere. Fixed SST experiments are run for 32 years each, the last 30 of which are used to quantify ERF and the ADJs/fast responses. Coupled ocean simulations are run for 90 years each, starting from a pre-spun-up preindustrial control simulation in year 321. The last 40 years of the coupled experiments—when the net TOA radiative flux stabilizes—are used to quantify climate impacts. The surface-temperature-mediated slow response is calculated as the difference between coupled ocean and fSST experiments⁴⁷. A 90-year coupled ocean simulation has not yet reached equilibrium, so we refer to these simulations as being in near equilibrium (computational cost restrictions prohibited longer integrations), similar to previous projects including PDRMIP^{22,48}. Our CESM2/CAM6 simulations do not include interactive chemistry; we therefore do not address possible atmospheric chemistry implications (for example, changes in ozone and stratospheric water vapour) or changes in methane lifetime.

Calculation of ADJs

The ADJs (for example, clouds, water vapour and temperature) in the climatological fixed SST experiments are estimated using the

radiative kernel method^{3,18,28,30,42}. Radiative kernels represent the radiative impacts from small perturbations in a state variable (for example, temperature, water vapour and surface albedo). Subsequently, ADJs can be computed by multiplication of the kernel with the response of the state variable. We use the Python-based radiative kernel toolkit (downloaded from ref.⁴⁹) and the Geophysical Fluid Dynamics Laboratory radiative kernel⁴⁹.

We use the same radiative kernel procedure to calculate the unnormalized (we do not divide by the change in global mean surface temperature) feedbacks. Specifically, surface-temperature-induced feedbacks are estimated by subtracting the ADJs (from fixed SST experiments) from the corresponding radiative kernel decomposition applied to the coupled experiments. Unnormalized feedbacks facilitate comparison with the ADJs.

ERF can be decomposed as $ERF = IRF + ADJ_{TT} + ADJ_{ST} + ADJ_{TS} + ADJ_{WV} + ADJ_{\alpha} + ADJ_C + \epsilon$, where ADJ_{TT} is the tropospheric temperature adjustment, ADJ_{ST} is the stratospheric temperature adjustment, ADJ_{TS} is the surface-temperature adjustment, ADJ_{WV} is the water-vapour adjustment, ADJ_{α} is the albedo adjustment, ADJ_C is the cloud adjustment and ϵ is the radiative kernel error. Individual ADJs are estimated as $ADJ_x = \frac{\partial R}{\partial x} dx$, where $\frac{\partial R}{\partial x}$ is the radiative kernel and dx is the response of state variable x as simulated by CESM2/CAM6. Kernels are four-dimensional (latitude, longitude, pressure and month) fields for atmospheric temperature and specific humidity and three-dimensional (latitude, longitude and month) fields for surface temperature and surface albedo. Two sets of kernels are used: clear-sky kernels, where the fluxes are calculated without clouds, and all-sky kernels.

As the radiative effect of clouds depends on several variables (fraction, ice and liquid-water content, droplet effective radius and so on), several approaches have been used to estimate cloud adjustments^{18,50}. Here we estimate cloud adjustments using the kernel difference method¹⁸, which involves a cloud-masking correction of cloud radiative-forcing diagnostics using the kernel-derived non-cloud adjustments and IRF according to $ADJ_C = (ERF - ERF_{cs}) - (IRF - IRF_{cs}) - \sum_{x=[T, TS, WV, \alpha]} (ADJ_x - ADJ_{x,cs})$, where subscript 'cs' refers to clear-sky quantities. Thus, the kernel difference method relies on the difference of all-sky and clear-sky kernel decompositions. See ref.¹⁸ for additional details.

The total ADJ is estimated as the sum of individual ADJs from the radiative kernel decomposition. Since we estimate IRF using PORT for all of our methane simulations, this can be used to estimate the radiative kernel error (ϵ) as $\epsilon = ERF - IRF - \sum_{x=[T, TS, WV, \alpha, C]} (ADJ_x)$. For example, the $10 \times CH_{4LW+SW}$ ERF and IRF are 1.69 and 2.08 W m^{-2} , yielding an $ERF - IRF$ difference of -0.39 W m^{-2} . The sum of the individual ADJs from the kernel decomposition is -0.40 W m^{-2} . Thus, the radiative kernel error for $10 \times CH_{4LW+SW}$ is 0.01 W m^{-2} . Similar results hold for $5 \times CH_{4LW+SW}$ and $2 \times CH_{4LW+SW}$, where ϵ is 0.03 W m^{-2} and -0.02 W m^{-2} , respectively. Relative to the corresponding ERFs, these errors are <1.0%, 3.1% and 5.7%, respectively. As ref.¹⁸ lacked an estimate of the IRF (which we estimate using PORT), they estimated ϵ under select situations (where the SW or LW IRF is known to be zero). In these situations, they found that the residual term is small, being “6%, 12% and 2% of the ERF for $10 \times BC_{LW}$, $3 \times CH_4_{SW}$ and $2 \times Solar_{LW}$ in magnitude, respectively. The larger multimodel residual in the $3 \times CH_4_{SW}$ case is biased by a large relative residual in the HadGEM2 model, whereas residuals in the other four models analysed are close to 0.” Thus, our radiative kernel errors are relatively small, and comparable to those estimated from select PDRMIP simulations¹⁸.

We note that methane IRF has an approximate square root dependency on concentration^{5,51}. PDRMIP $3 \times CH_4$ simulations yield a $3 \times CH_4$ IRF of $1.1 \pm 0.24 \text{ W m}^{-2}$, but nearly all of the PDRMIP models used year 2000 as the base year. This perturbation is thus similar to $5\text{--}6 \times$ preindustrial CH_4 (our $5 \times CH_4$ IRF is 1.18 W m^{-2} , with 0.14 W m^{-2} due to SW radiative effects).

Statistical significance

Statistical significance of a climate response is calculated using a two-tailed pooled t test. An annual mean time series is calculated for both the perturbation experiment and the preindustrial base experiment (for example, at individual grid boxes or averaged globally), and their difference is taken. The null hypothesis of a zero difference is evaluated, with $n_1 + n_2 - 2$ degrees of freedom, where n_1 and n_2 are the number of years in the perturbation experiment and base (30 years for fSST experiments; 40 years for coupled ocean experiments). Here, the pooled variance, $\frac{(n_1-1)S_1^2 + (n_2-1)S_2^2}{n_1+n_2-2}$, is used, where S_1 and S_2 are the sample variances.

A similar procedure is used to quantify statistical significance of the radiative flux perturbations and rapid adjustments (for example, Fig. 2). These uncertainties are therefore relative to interannual variability and do not account for possible intermodel or kernel uncertainties (as in ref.¹⁸, using 10+ PDRMIP models). As we have only one year of data for the IRF, we evaluate its uncertainty relative to the preindustrial base experiment with fixed SSTs. Nearly all of our ADJs under $10 \times CH_4$ are significant at the 90% confidence level (the lone exception is the surface-temperature adjustment under $10 \times CH_{4SW}$). Similar conclusions also hold for $5 \times CH_4$ (Extended Data Fig. 4d). Under $2 \times CH_4$, however, most of the ADJs under $2 \times CH_{4SW}$ are not significant (Extended Data Fig. 4g), including the total ADJ. This is consistent with the relatively small $2 \times CH_4$ SW IRF of 0.04 W m^{-2} .

We also find similar results using an alternative kernel (CloudSat/CALIPSO; Extended Data Fig. 5), so our ADJ conclusions are robust across these two kernels. Finally, we note that the ADJs in PDRMIP models that include CH_4 SW absorption (under $3 \times CH_4$, which is a perturbation similar to our $5 \times$ preindustrial CH_4) are all significant at the 95% confidence level¹⁸, and this includes the intermodel and kernel uncertainty.

Data availability

PDRMIP simulations can be accessed at <https://cicero.oslo.no/en/PDRMIP/PDRMIP-data-access>. A core set of model data from our idealized methane CESM2 simulations can be downloaded from Zenodo at <https://doi.org/10.5281/zenodo.7596623>.

Code availability

The Python-based radiative kernel toolkit and the GFDL radiative kernel can be downloaded from <https://climate.rsmas.miami.edu/data/radiative-kernels/>.

References

- Conley, A. J., Lamarque, J.-F., Vitt, F., Collins, W. D. & Kiehl, J. PORT, a CESM tool for the diagnosis of radiative forcing. *Geosci. Model Dev.* **6**, 469–476 (2013).
- Clough, S. A. et al. Atmospheric radiative transfer modeling: a summary of the AER codes. *J. Quant. Spectrosc. Radiat. Transf.* **91**, 233–244 (2005).
- Iacono, M. J. et al. Radiative forcing by long-lived greenhouse gases: calculations with the AER radiative transfer models. *J. Geophys. Res. Atmos.* **113**, D13103 (2008).
- Forster, P. M. et al. Recommendations for diagnosing effective radiative forcing from climate models for CMIP6. *J. Geophys. Res. Atmos.* **121**, 12460–12475 (2016).
- Sherwood, S. C. et al. Adjustments in the forcing-feedback framework for understanding climate change. *Bull. Am. Meteorol. Soc.* **96**, 217–228 (2015).
- Smith, C. J. et al. Effective radiative forcing and adjustments in CMIP6 models. *Atmos. Chem. Phys.* **20**, 9591–9618 (2020).
- Pincus, R., Barker, H. W. & Morcrette, J.-J. A fast, flexible, approximate technique for computing radiative transfer in inhomogeneous cloud fields. *J. Geophys. Res. Atmos.* <https://doi.org/10.1029/2002JD003322> (2003).

44. Hogan, R. J. & Matricardi, M. Evaluating and improving the treatment of gases in radiation schemes: the Correlated K-Distribution Model Intercomparison Project (CKDMIP). *Geosci. Model Dev.* **13**, 6501–6521 (2020).
45. Lawrence, D. M. et al. The Community Land Model version 5: description of new features, benchmarking, and impact of forcing uncertainty. *J. Adv. Model. Earth Syst.* **11**, 4245–4287 (2019).
46. Neale, R. B. et al. *Description of the NCAR Community Atmosphere Model (CAM 5.0)* Technical Report NCAR/TN-486+STR (NCAR, 2012).
47. Samset, B. H. et al. Fast and slow precipitation responses to individual climate forcings: a PDRMIP multimodel study. *Geophys. Res. Lett.* **43**, 2782–2791 (2016).
48. Myhre, G. et al. Scientific data from precipitation driver response model intercomparison project. *Sci. Data* **9**, 123 (2022).
49. Soden, B. J. et al. Quantifying climate feedbacks using radiative kernels. *J. Clim.* **21**, 3504–3520 (2008).
50. Zelinka, M. D., Klein, S. A. & Hartmann, D. L. Computing and partitioning cloud feedbacks using cloud property histograms. Part I: cloud radiative kernels. *J. Clim.* **25**, 3715–3735 (2012).
51. Ramaswamy, V. et al. in *Climate Change 2001: The Scientific Basis* (eds Houghton, J. T. et al.) Ch. 6 (Cambridge Univ. Press, 2001).

Acknowledgements

R.J.A. is supported by NSF grant AGS-2153486 and the Research Council of Norway Project no. 324182. R.J.K. is supported by NASA Science of Terra, Aqua and Suomi-NPP grant no. 80NSSC21K1968 and NOAA grant no. NA18OAR4310269. We acknowledge high-performance computing support from Cheyenne (<https://doi.org/10.5065/D6RX99HX>) provided by NCAR's Computational

and Information Systems Laboratory, sponsored by the National Science Foundation.

Author contributions

R.J.A. conceived the project, designed the study, performed simulations and analyses and wrote the paper. X.Z. performed preliminary simulations. C.A.R., R.J.K., C.J.S. and B.H.S. advised on methods and data interpretation. All authors discussed results and contributed to the writing of the paper.

Competing interests

The authors declare no competing interests.

Additional information

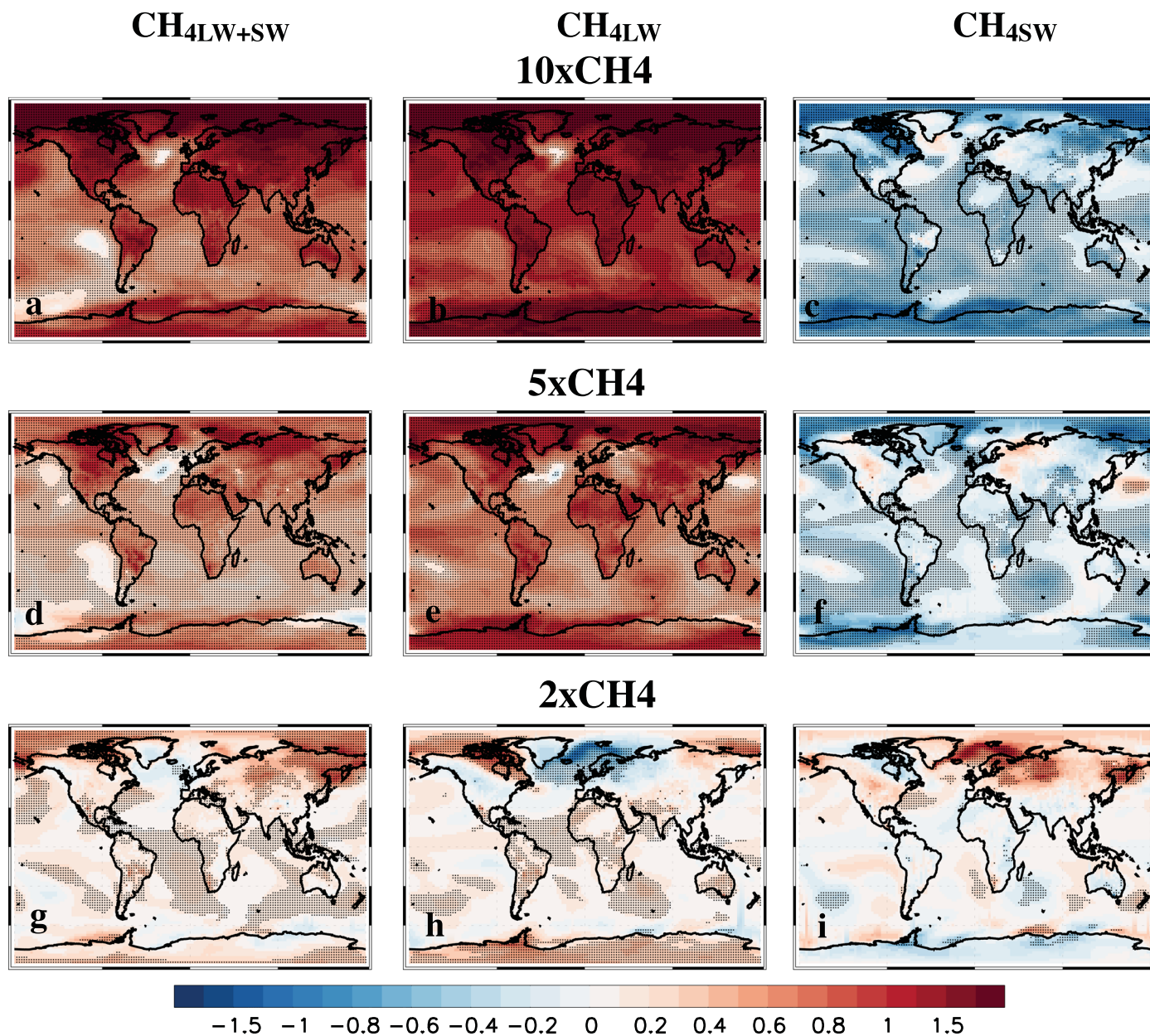
Extended data is available for this paper at <https://doi.org/10.1038/s41561-023-01144-z>.

Supplementary information The online version contains supplementary material available at <https://doi.org/10.1038/s41561-023-01144-z>.

Correspondence and requests for materials should be addressed to Robert J. Allen.

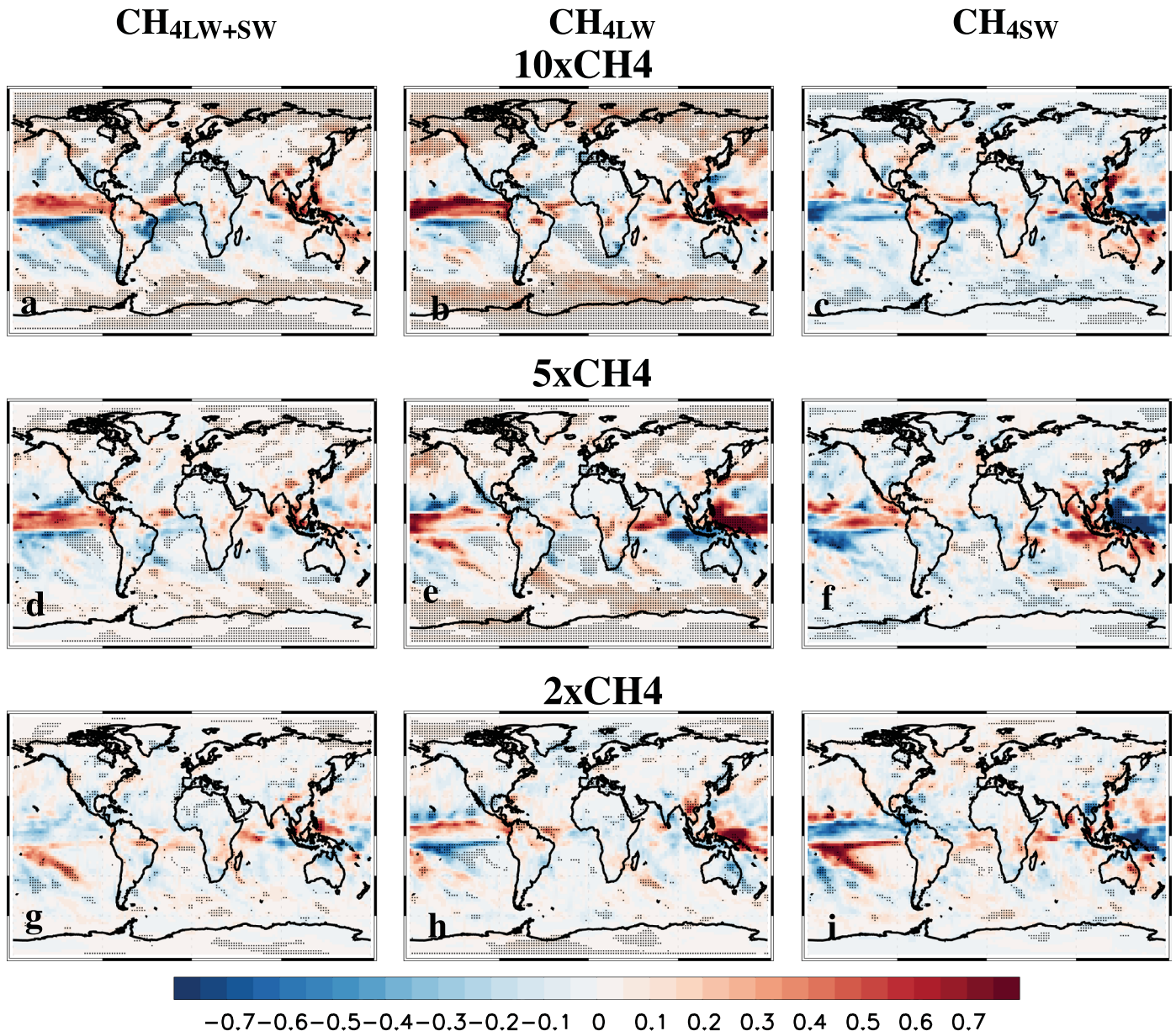
Peer review information *Nature Geoscience* thanks the anonymous reviewers for their contribution to the peer review of this work. Primary Handling Editor: Xujia Jiang, in collaboration with the *Nature Geoscience* team.

Reprints and permissions information is available at www.nature.com/reprints.

Δ Near-Surface Air Temperature [K]

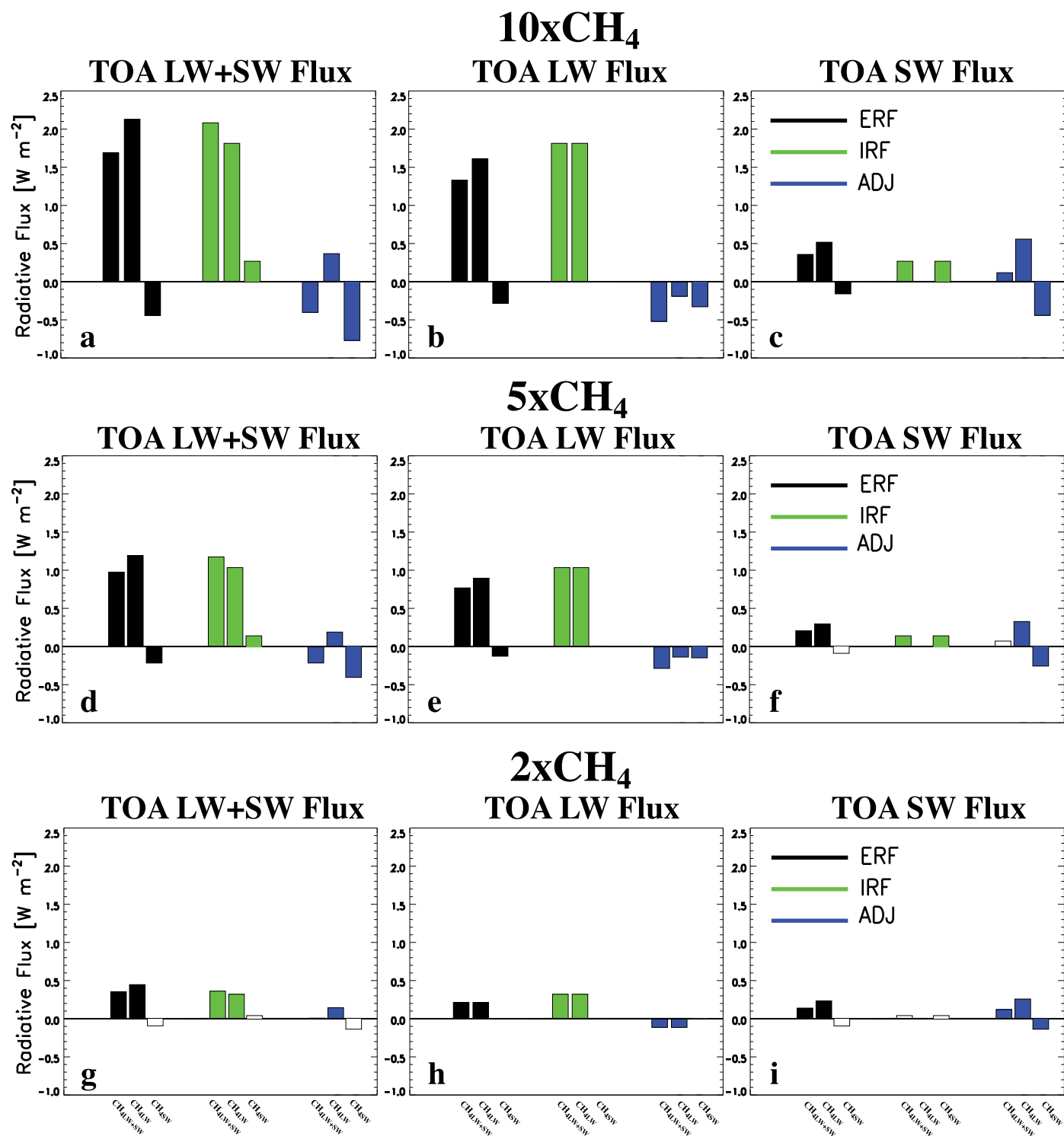
Extended Data Fig. 1 | Global maps of the total near-surface air temperature response to methane perturbations. Annual mean near-surface air temperature response for (a-c) 10xCH₄, (d-f) 5xCH₄ and (g-i) 2xCH₄ decomposed into (a, d, g) CH_{4LW+SW}, (b, e, h) CH_{4LW} and (c, f, i) CH_{4SW}. Units are K. Solid dots

represent a significant response at the 90% confidence level, based on a standard t-test. Climate responses are estimated from the coupled simulations, which include the IRF, adjustments and feedbacks.

Δ Precipitation [mm day^{-1}]

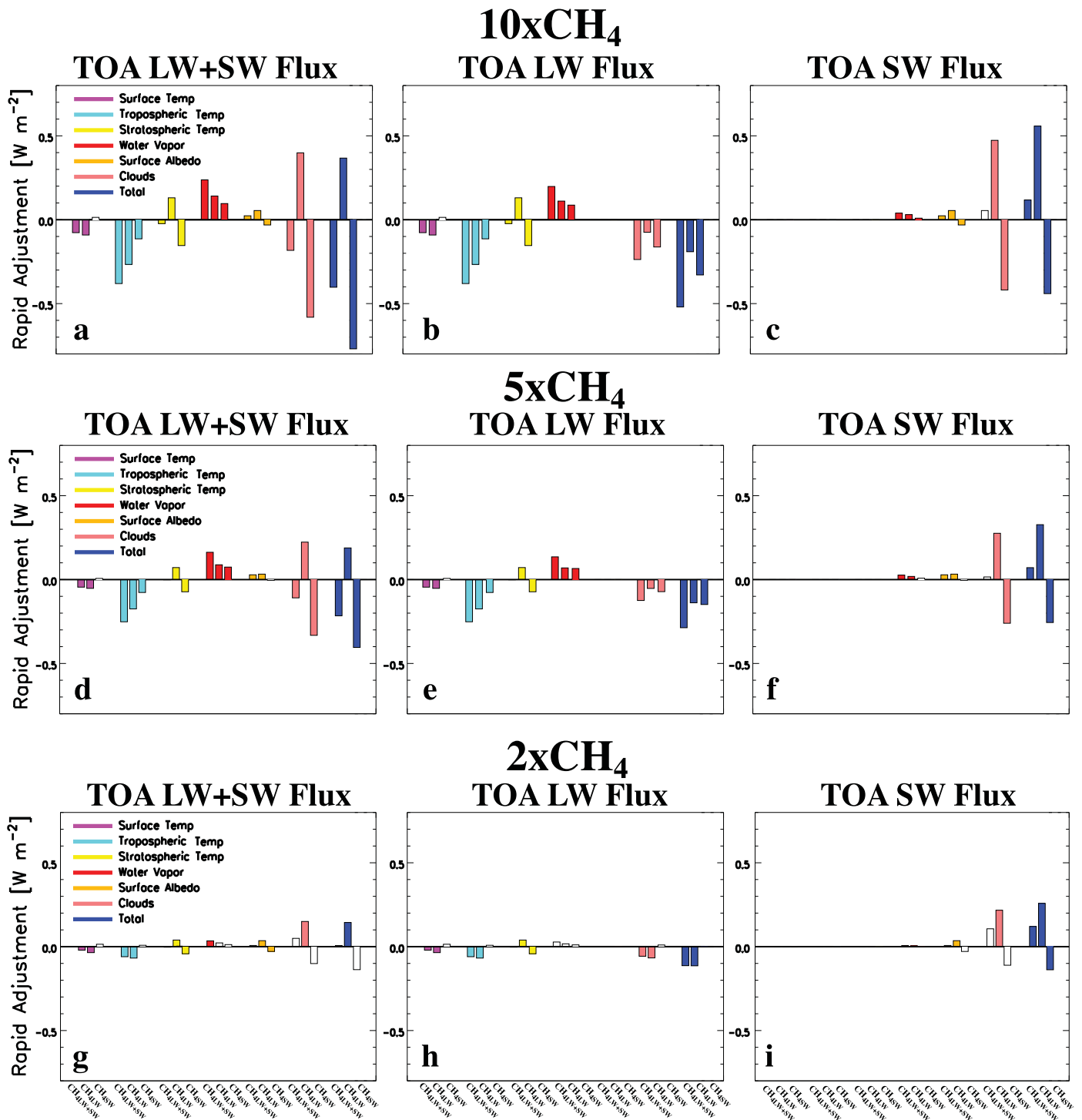
Extended Data Fig. 2 | Global maps of the total precipitation response to methane perturbations. Annual mean precipitation response for (a-c) $10\times\text{CH}_4$, (d-f) $5\times\text{CH}_4$ and (g-i) $2\times\text{CH}_4$ decomposed into (a, d, g) $\text{CH}_4_{\text{LW+SW}}$, (b, e, h) CH_4_{LW} and (c, f, i) CH_4_{SW} . Units are mm day^{-1} . Solid dots represent a significant response

at the 90% confidence level, based on a standard t-test. Climate responses are estimated from the coupled simulations, which include the IRF, adjustments and feedbacks.



Extended Data Fig. 3 | Top-of-the-atmosphere radiative flux components in response to methane perturbations. Global annual mean top-of-the-atmosphere (TOA) effective radiative forcing (ERF; black), instantaneous radiative forcing (IRF; green) and rapid adjustment (ADJ; blue) for (a-c) $10\times\text{CH}_4$, (d-f) $5\times\text{CH}_4$ and (g-i) $2\times\text{CH}_4$ for (a, d, g) LW+SW, (b, e, h) LW and (c, f, i) SW radiative fluxes. The first bar in each like-colored set of three bars represents the contribution from $\text{CH}_{4\text{LW+SW}}$; the second bar represents $\text{CH}_{4\text{LW}}$; and the third

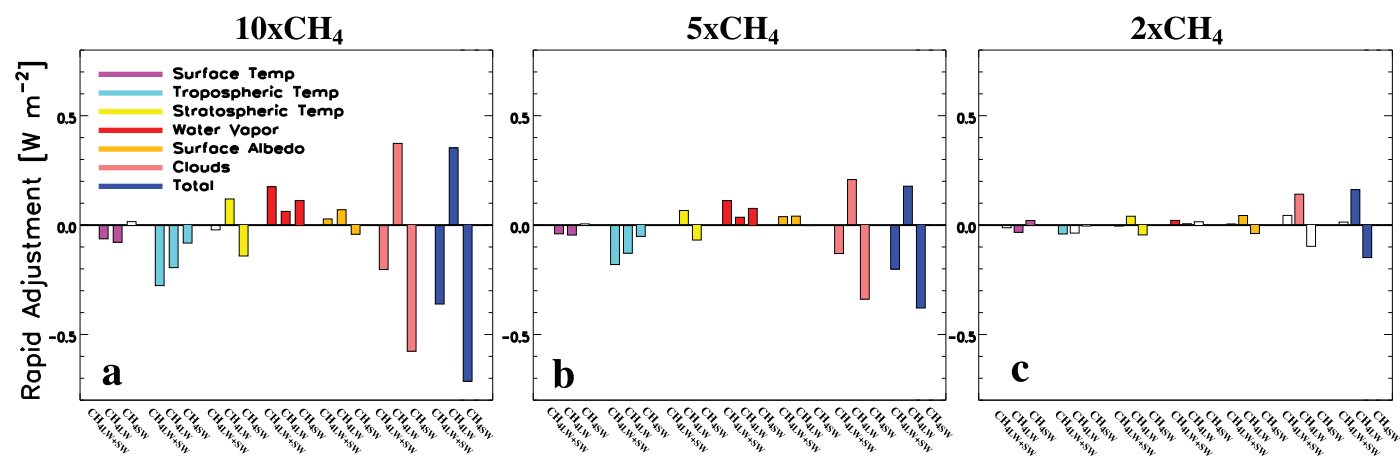
represents $\text{CH}_{4\text{SW}}$. Responses not significant, based on a standard t-test at the 90% confidence level, have unfilled bars. These uncertainties are therefore relative to interannual variability. Units are W m^{-2} . ERF is estimated as the net TOA energy imbalance from the fixed SST experiments. IRF is estimated using an offline radiative transfer model, PORT. The total rapid adjustment is estimated as the sum of individual rapid adjustments from the radiative kernel decomposition. Panel (a) is identical to Fig. 2a from the main paper.



Extended Data Fig. 4 | Top-of-the-atmosphere rapid adjustment decomposition in response to methane perturbations. Global annual mean top-of-the-atmosphere (TOA) surface temperature (purple), tropospheric temperature (cyan), stratospheric temperature (yellow), water vapor (red), surface albedo (orange), cloud (pink) and total (blue) rapid adjustment for (a-c) $10\times\text{CH}_4$, (d-f) $5\times\text{CH}_4$ and (g-i) $2\times\text{CH}_4$ for (a, d, g) LW+SW, (b, e, h) LW and (c, f, i) SW radiative fluxes. The first bar in each like-colored set of three bars represents the

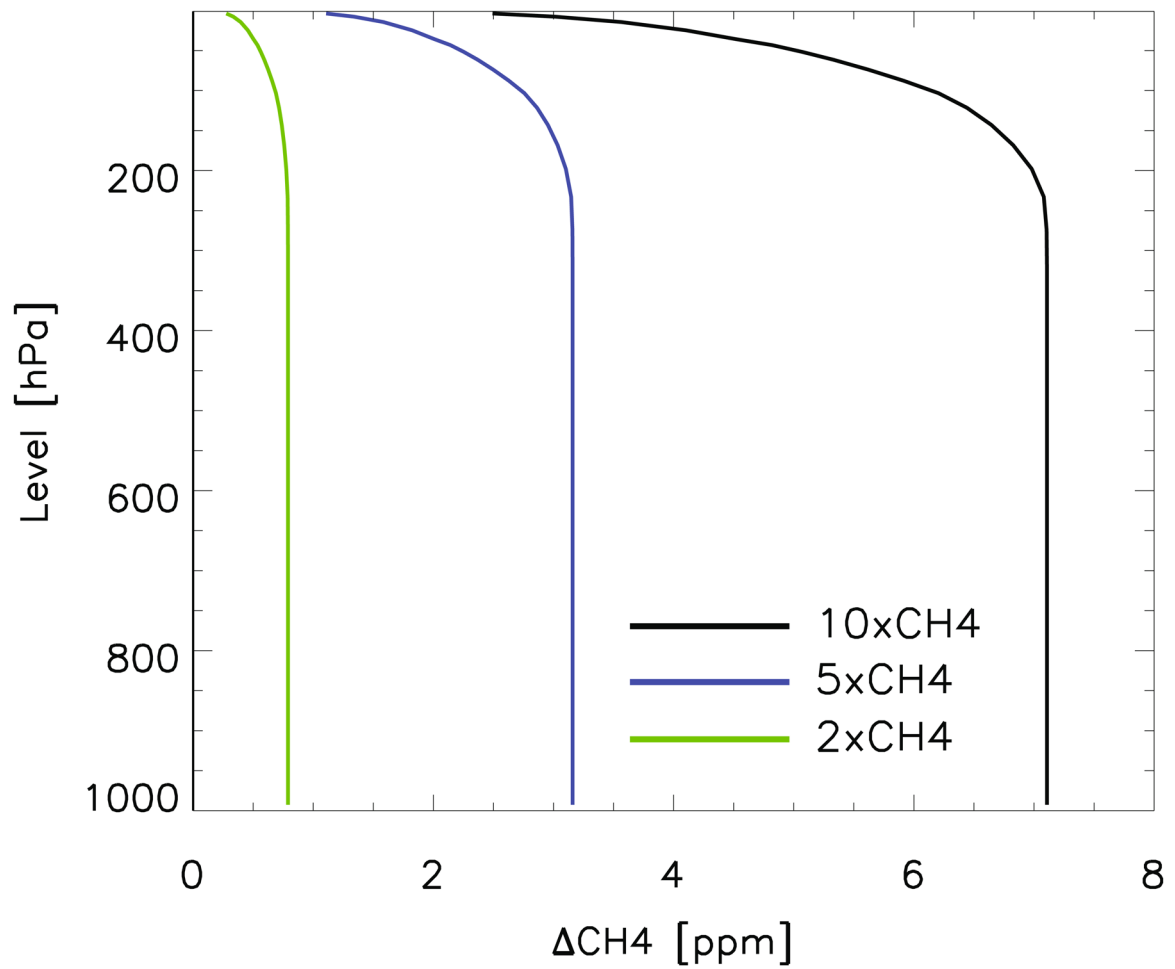
contribution from $\text{CH}_{4\text{LW+SW}}$; the second bar represents $\text{CH}_{4\text{LW}}$; and the third bar represents $\text{CH}_{4\text{SW}}$. Responses not significant, based on a standard t-test at the 90% confidence level, have unfilled bars. These uncertainties are therefore relative to inter-annual variability. Rapid adjustments are estimated from the radiative kernel decomposition applied to the fixed SST experiments. Units are W m^{-2} . Panel (a) is identical to Fig. 2b from the main paper.

TOA Rapid Adjustments (CloudSat/CALIPSO Kernel)

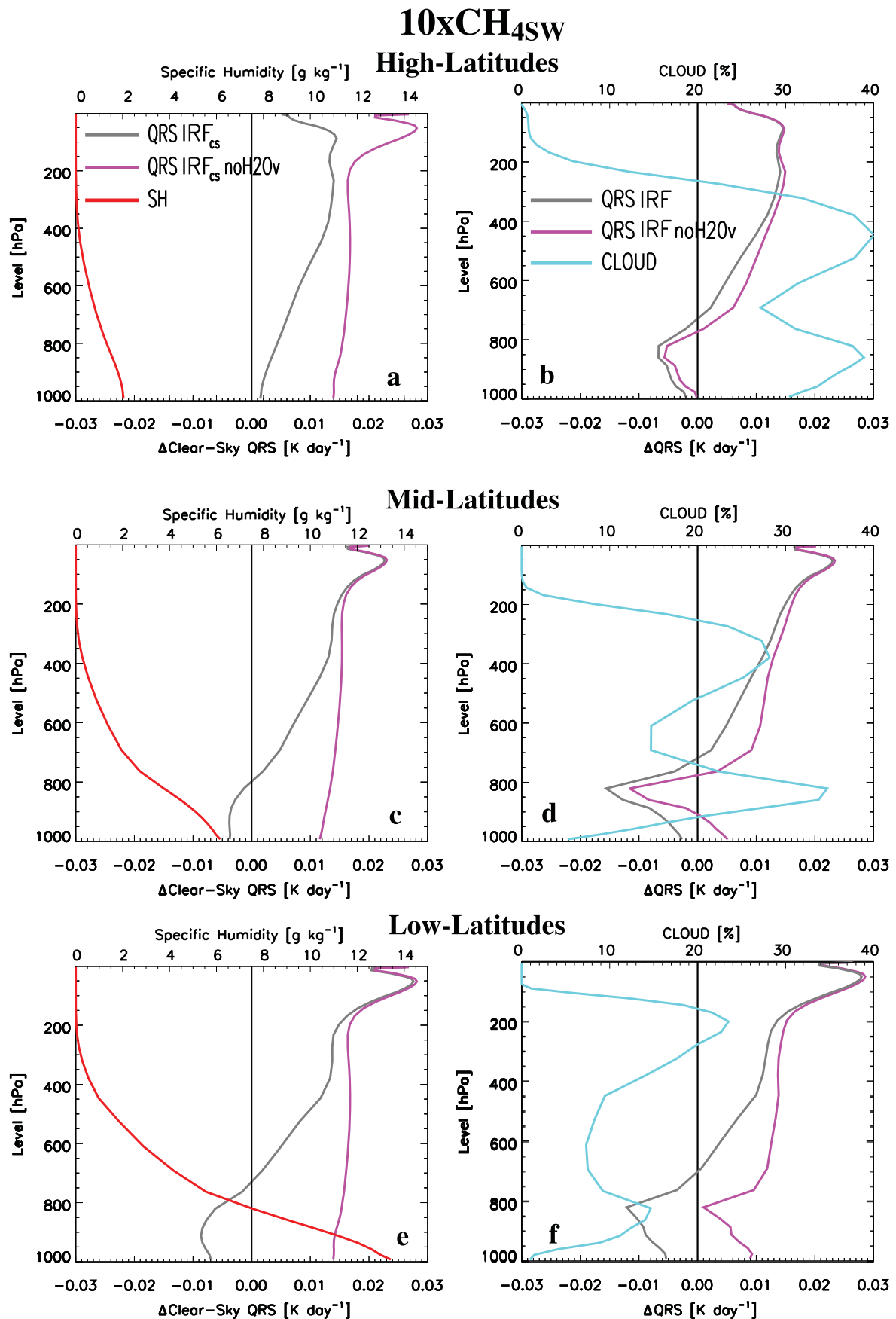


Extended Data Fig. 5 | Top-of-the-atmosphere rapid adjustment decomposition using CloudSat/CALIPSO radiative kernels. Global annual mean top-of-the-atmosphere (TOA) surface temperature (purple), tropospheric temperature (cyan), stratospheric temperature (yellow), water vapor (red), surface albedo (orange), cloud (pink) and total (blue) rapid adjustment for (a) $10\times\text{CH}_4$, (b) $5\times\text{CH}_4$, and (c) $2\times\text{CH}_4$. The first bar in each like-colored set of three

bars represents the contribution from $\text{CH}_{4\text{LW}+\text{SW}}$; the second bar represents $\text{CH}_{4\text{LW}}$; and the third bar represents $\text{CH}_{4\text{SW}}$. Responses not significant, based on a standard t-test at the 90% confidence level, have unfilled bars. These uncertainties are therefore relative to interannual variability. Units are W m^{-2} . The total rapid adjustment is estimated as the sum of individual rapid adjustments from the radiative kernel decomposition.



Extended Data Fig. 6 | Global annual mean vertical profiles of the atmospheric methane concentration perturbation. Atmospheric CH₄ concentration [ppm] for 10xCH₄ (black), 5xCH₄ (blue) and 2xCH₄ (green) relative to preindustrial CH₄.

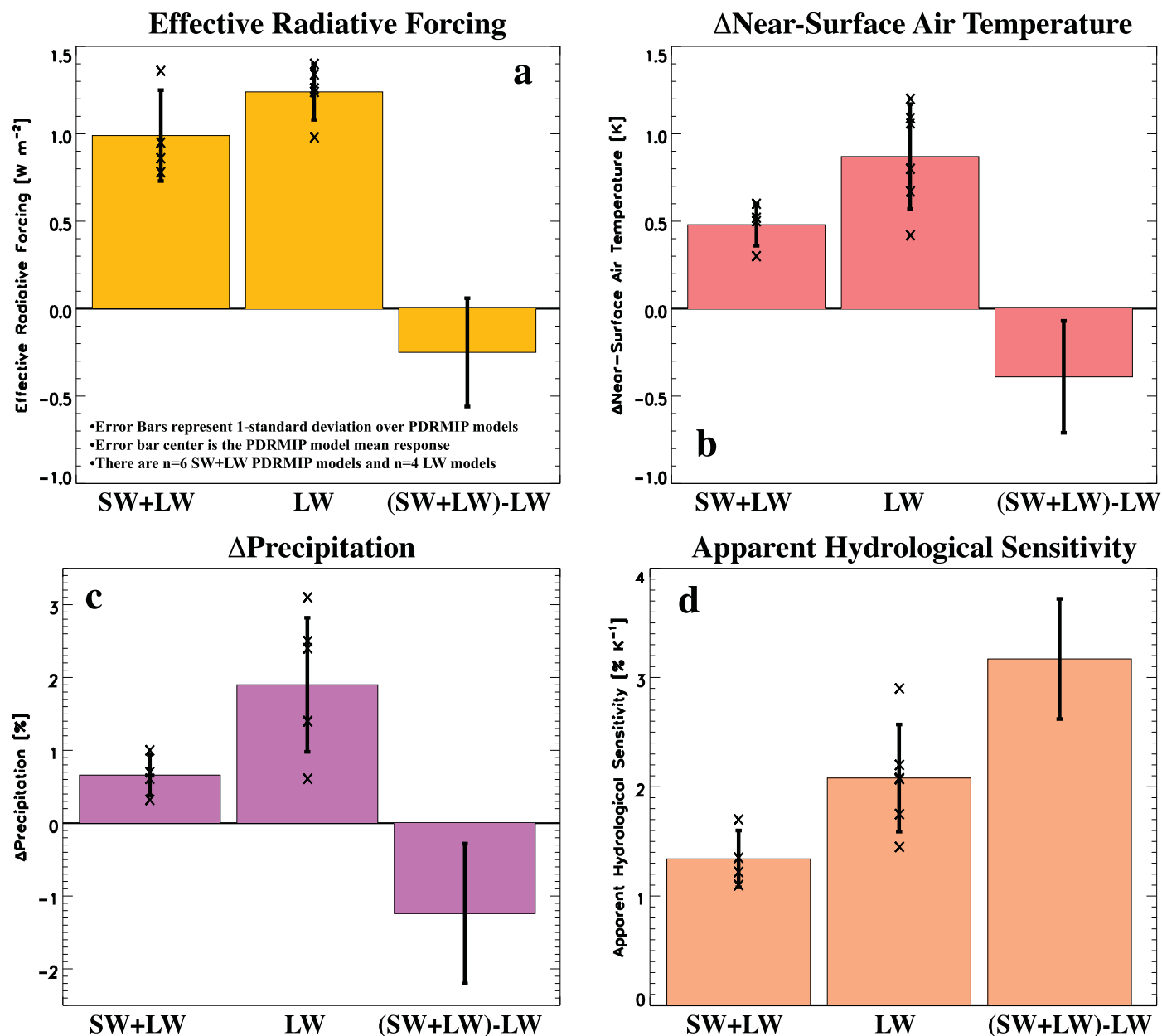


Extended Data Fig. 7 | See next page for caption.

Extended Data Fig. 7 | Regional annual mean vertical profiles of instantaneous heating rate for $10\times\text{CH}_4$ SW. As in Fig. 4 from the main paper (which is based on the global annual mean), but broken down into the (a, b) high-latitude annual mean; (c, d) mid-latitude annual mean; and (e, f) low-latitude annual mean. Instantaneous atmospheric (a, c, e) clear-sky shortwave heating rate (QRS IRF_{cs}; gray) and the corresponding clear-sky shortwave heating rate without water vapor shortwave absorption (QRS IRF_{cs} noH₂O_v; purple) in the same three near-infrared bands (1.6–1.9, 2.15–2.5 and 3.1–3.85 μm) that methane

absorbs in. Instantaneous atmospheric (b, d, f) all-sky (that is, with clouds) shortwave heating rate (QRS IRF; gray) and the corresponding shortwave heating rate without water vapor shortwave absorption (QRS IRF noH₂O_v; purple) in the same three near-infrared bands that methane absorbs in. Also included in (a, c, e) is the climatological specific humidity (SH; red) and in (b, d, f) the climatological cloud fraction (CLOUD; cyan). QRS IRF, QRS IRF_{cs}, CLOUD and SH units are K day^{-1} , K day^{-1} , % and g kg^{-1} , respectively.

PDRMIP 3xCH₄ Results



Extended Data Fig. 8 | 3xCH₄, PDRMIP results. Global annual mean (a) effective radiative forcing (ERF), (b) near-surface air temperature response, (c) precipitation response, and (d) apparent hydrological sensitivity to 3xCH₄ from PDRMIP experiments. The first bar in each like-colored set of three bars represents 4 models that include methane LW and SW radiative effects; the second bar represents 6 models that include the methane LW radiative effect; and the third bar represents the difference (that is, an indirect estimate of

the methane SW radiative effects). Error bars show the 1-standard deviation uncertainty across models (added in quadrature for the third bar). This includes 4 models for methane LW and SW radiative effects and 6 models for methane LW radiative effects. Units in (a) are W m⁻²; units in (b) are K; units in (c) are %; and units in (d) are % K⁻¹. ERF comes from PDRMIP fSST simulations; remaining responses are estimated from the coupled simulations. Symbols (X's) in the first two sets of bars for each panel represent individual PDRMIP models.